The following publication Hu, Y., Zhong, H., Wang, Y., Lu, L., & Yang, H. (2018). TiO2/antimony-doped tin oxide: Highly water-dispersed nano composites with excellent IR insulation and super-hydrophilic property. Solar Energy Materials and Solar Cells, 174, 499-508 is available at https://doi.org/10.1016/j.solmat.2017.09.027.

# $TiO_2$/antimony-doped tin oxide: Highly water-dispersed nano composites with excellent IR insulation and super-hydrophilic property

*Yan Hu[a], Yuanhao Wang[b*], Lin Lu[a], Hongxing Yang[a**] and Yinting Wong[c]*

*a Renewable Energy Research Group (RERG), Department of Building Services Engineering, The Hong Kong Polytechnic University, Hong Kong*

*b Faculty of Science and Technology, Technological and Higher Education Institute of Hong Kong, New Territories, Hong Kong*

*c Department of Biomedical Science, City university of Hong Kong, Kowloon Tong, Hong Kong*

** Corresponding author: yuanhaowang@yahoo.com*

*** Corresponding author: hong-xing.yang@polyu.edu.hk*

**Keywords**: Titanium dioxide; Highly water-dispersed; ATO; IR insulation; Heat insulation.

## Abstract

In this work, a novel aqueous self-dispersed $TiO_2$ is synthesized and then used to produce the highly water-dispersed ATO/$TiO_2$ composite particles, which has strong IR insulation property. Thus, it can be used to block the solar radiative heat transfer in a building. The primary particle size of ATO/$TiO_2$ composites detected by TEM ranges from 5~12 nm,

but the pure ATO particles is more than 2 μm. A small amount of $TiO_2$ (16.7% wt) increases the Zeta potential in water from 6.7 mV to 37.01 mV, which represents the stability is largely enhanced. The IR transmittance in IR band is decreased from ca. 90% (original glass) to ca. 1% (ATO 83.33% wt). The thermal performances of glass with such coatings are simulated based on Hong Kong climate situation. For the best sample, the electricity used in air-conditioning and lighting is 27% less than uncoated glass. Furthermore, the $TiO_2$ makes the water contact angle of the coating ranging from 3~5.6°. Therefore, the coating film can be prevented from fouling due to super-hydrophilicity and have longer lift time.

# 1. Introduction

For a commercial building or a dwelling, the energy spent in cooling is about 42~68% of the total energy consumption. [1] Decreasing the cooling load is quite important to save the building energy consumption. Most of the heat comes from the radiative heat transfer of the sunlight, in which, in terms of energy, the UV light (below 400nm) is about 3~5 %, the visible light (400~700 nm) is about 42~43 % and IR ray (above 700 nm) is about 52~55%. [2] IR ray has the strongest heat effect, thus for an energy saving coating, the IR ray must be blocked. Besides, the visible light should not be influenced otherwise the lighting in a building is negatively influenced.

The transparent IR insulation coating is a special one which does not block the visible light but insulate the IR ray and obstruct most of the radiative heat transfer.

Antimony-doped tin oxide (ATO), Indium tin oxide (ITO) etc. are materials with the visible light transmittance and IR blocking property. [3] However, because of the cost issue, ITO cannot be widely applied.

ATO has been widely used because of the lower price. ATO film shows highly visible light transmittance, IR shielding (including near-IR absorption and far-IR reflection) properties. [4-11] To obtain ATO films with high electrical and optical property, the particle size should be in nano-scale and it must be highly dispersed. Basically, there are several methods to synthesize nano-ATO particles: solid-phase synthesis [12], co-precipitation synthesis [13], sol-gel synthesis [14], hydrothermal synthesis [15] and Pechini synthesis [16] etc. However, after the synthesis of nano-ATO, for the further application, it must be well-dispersed in specific solvent, otherwise the aggregation influences the optical and electrical property negatively. Initially, the most used dispersion system is oil-based solution [17], which emits a lot of VOC during practical application. However, with the population of the environment friendly concept, the oil-based solution gradually fading out. A lot of researches are focused on the environmental water-based solutions. In this area, silane coupling agents are often selected as the dispersing agents [18-20] because they are the most commonly used chemical agents. Besides, titanate coupling agents are also applied as the dispersing agent [21]. They indeed increased the dispersity of ATO after the high shear force dispersion process. However, to achieve the highly dispersion no matter in water phase or in organic phase, they still need a lot of organic materials, such as the organic dispersing agents or

some organic solvent for the pre-dispersion. In this work, a novel approach which use self-made inorganic self-dispersed $TiO_2$ as the aqueous dispersing agent was applied and then a water-dispersed ATO/$TiO_2$ particle is synthesized.

$TiO_2$ is a widely used inorganic material. It can be used in photo-catalysis [22,23], self-cleaning [24,25], solar cell and sensor fabrication [26], environmental applications [27] and energy storage [28] etc. In this paper, a highly water-dispersed $TiO_2$ nano particle is firstly synthesized. Then, it is ball-milled with ATO particles and water is the dispersing agent. After this step, the ATO particles and $TiO_2$ are mixed uniformly. The hydroxyl groups on their surface are condensed so that they are combined tightly. Thus, with the help of highly water-dispersed $TiO_2$, the water based colloid is obtained. Besides that, with the application of $TiO_2$, the ATO film has extra super-hydrophilic self-cleaning property. It is helpful to keep the surface clean and then the optical properties of ATO coating can also be maintained. Besides, the energy saving effect of those coating is compared through simulation.

# 2. Experiments

## 2.1. Materials

In this work, the titanium tetrachloride, ethyl alcohol, tin tetrachloride, antimony chloride and hydrochloric acid (37%) are brought from Sigma-Aldrich. They are of analytical grade and do not need further purification.

## 2.2. Procedures of Experiments

The highly water-dispersed $TiO_2$ is firstly synthesized via solvent-thermal method. 10 ml titanium tetrachloride and 80 ml absolute ethanol are mixed uniformly. Then they are solvent-thermal synthesized in 180 ℃ for 6 h. The highly water-dispersed $TiO_2$ is obtained after being filtered and dried. Following that, the ATO particles are synthesized. $SnCl_4 \cdot 5H_2O$ and $SbCl_2$ are dispersed in hydrochloric acid (37%) separately since they are quite easy to deliquesce in air. Then, they are mixed in the ratio of Sn:Sb=9:1 (mol). The solution is adjusted to pH 10. After a 24 h stirring, the final solution is transferred to the hydrothermal reactor. It is heated to 200 ℃ for 24 h. The powder is obtained after filtration and drying in 100 ℃ for 10 h. Then, the ATO particles are finally obtained after the thermal treatment at 600 ℃ for 6 h.

Following that, the ball-milling samples are prepared based on Table. 1. All the samples are ball-milled in 3000 r/min rotation speed for 12 h. The samples are collected via water washing. Then they were all condensed to the solid content of 5.0% under 50 ℃.

Table. 1 Seven samples with different ATO mass fraction but constant DI water.

| Sample No. | 1 | 2 | 3 | 4 | 5 | 6 | 7 |
|---|---|---|---|---|---|---|---|
| ATO/g | 0 | 1 | 2 | 3 | 4 | 5 | 6 |
| $TiO_2$/g | 6 | 5 | 4 | 3 | 2 | 1 | 0 |
| ATO concentration/% | 0 | 16.67 | 33.33 | 50.00 | 66.67 | 83.33 | 100 |
| DI Water/ml | 10 | | | | | | |

# 3. Characterizations

The ball miller selected in this work is Planetary Mono Mill PULVERISETTE 6 from Fritsch. The tube furnace used is RD 30/200/11 from Nabertherm. The X-ray diffraction (XRD) tests are conducted by the Rigaku highly versatile multipurpose X-ray diffraction system with Cu Kα radiation (λ=0.15406nm) and 2θ ranging from 10° to 90°. The transmission electron microscopy (TEM) pictures are obtained by the JEM-2100F from JEOL. The XPS characterizations are conducted by Thermo Scientific ESCALAB XI+ X-ray Photoelectron Spectrometer (XPS) Microprobe. The FT-IR tests are all processed by Nicolet$^{TM}$ iS$^{TM}$ 50 FT-IR Spectrometer from Thermo Scientific. The thermogravimetric analysis (TGA) is conducted via Netzsch 449. The particle distribution results are obtained by the Mastersizer 3000 from Malvern. The Zeta potential results are gotten via Nano ZS from Malvern. The electrical conductivities are measured by a Hall effect measurement system (Hall 5500). The coating thickness results are obtained by Surface Profiler Tencor P-10. The contact angle tests are proceeded by Contact Angle Goniometer Sindatek Model 100SB from SINDATEK. The Vis-NIR characterizations are processed by Hitachi U-4100 from Hitachi. The simulation software is Energy Plus 8.3. The climate data of Hong Kong is used.

# 4. Results and discussions

## 4.1. The XRD characterizations

The XRD patterns of samples in Table. 1 are shown in Fig. 1. As displayed in this figure, Sample 1 is the self-dispersed $TiO_2$ and it matches the standard anatase $TiO_2$

(PDF#89-4921) pattern perfectly. In Sample 7, which represents the original ATO sample, there are no detectable peaks appearing when compared with standard $SnO_2$ (PDF#41-1445). Thus, the lattice does not change, which further demonstrates Sb is doped in the $SnO_2$ and forms substitutional or interstitial solid solution.

From Sample 2 to Sample 6, the characteristic peaks of $SnO_2$ are obvious. For example, the (110), (101), (200), (211), (220), (310) and (301) lattice planes locate at 26.6°, 33.9°, 37.9°, 51.8°, 54.8°, 61.8° and 65.9° respectively. With the increase of ATO concentration, the peaks strength, such as (110), (101) and (211), gains too. This reflects the ATO crystallization become better and better. Furthermore, based on Debye-Scherrer formula [29] in equation (1), the crystal particle size could be calculated approximately.

$$\mathrm{D} = \frac{K\gamma}{B\cos\theta} \tag{1}$$

In this formula, D represents the grain crystal average thickness in the direction perpendicular to the crystal face, namely the crystal particle size; K represents the Scherrer constant (if B is the full wave at half maximum, K=0.89 and if B is the integral wave wide, K=1); γ represents the wavelength of X-ray, which is 0.154056 nm and θ is the diffraction angle. Moreover, B and θ must be in radian. Therefore, given the strongest peaks in Fig. 1, the grain size from Sample 1 to Sample 7 are calculated and listed in Table. 2.

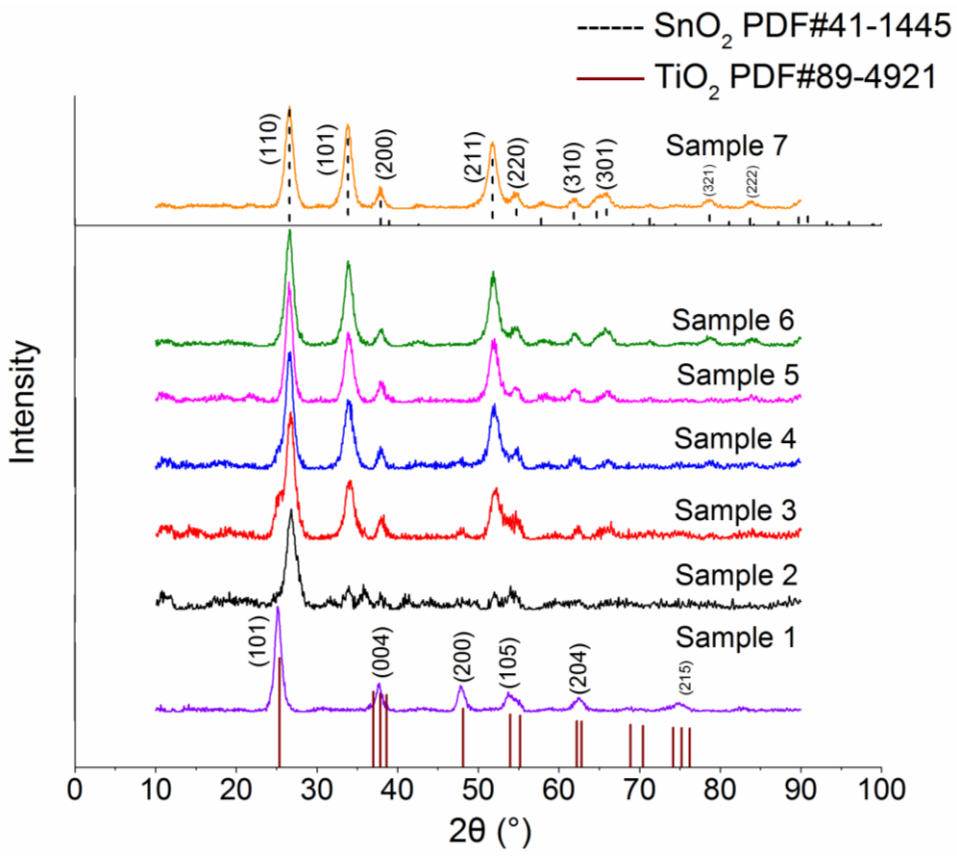


Fig. 1 The XRD patterns from Sample 1 to Sample 7.

As displayed in Table. 2, the calculated grain size ranges from 5~10 nm. However, they are just approximate results and the practical value must be obtained from further measurements, such as the TEM or the particle distribution meter. Nevertheless, there are no obvious characteristic peaks of anatase $TiO_2$ are displayed from Sample 2 to Sample 6 in Fig. 1. TEM characterizations are conducted for further investigation.

Table. 2 The calculated grain size based on the Debye-Scherrer formula from Sample 1 to Sample 7.

| Sample No. | 1 | 2 | 3 | 4 | 5 | 6 | 7 |
|---|---|---|---|---|---|---|---|
| D/nm | 9.54 | 5.67 | 6.23 | 8.6 | 6.76 | 7.57 | 6.76 |

## 4.2. The EDS and TEM characterizations

The EDS and TEM results are all shown in Fig. 2. Firstly, for the EDS results, since those nano particles are supported by the carbon membrane and copper net during the TEM tests, the C and Cu peaks in EDS patterns are eliminated. From the EDS patterns below, there are only Ti, Sn, Sb and O existing in those samples. In Sample 1, only Ti and O are detected since it is the $TiO_2$. Starting from Sample 2, the Sn and Sb appear and their peak strength increase. At the same time, the strength of Ti decreases until totally disappears in Sample 7, which represents the ATO particles.

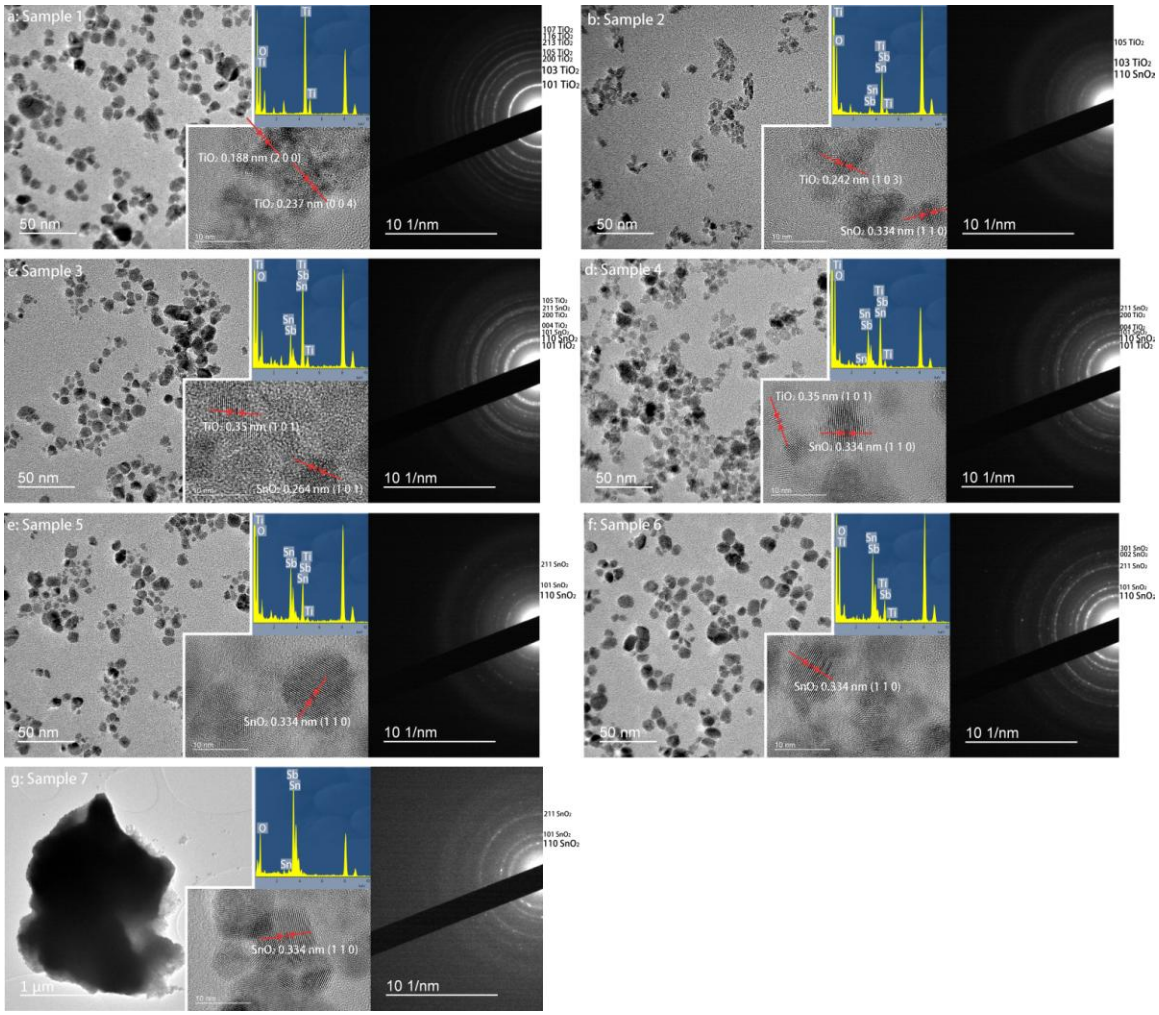


Fig. 2 The EDS, TEM, SAED and HR TEM images form Sample 1 to Sample 7

Secondly, the TEM, SAED and HRTEM results are analyzed. As shown in TEM pictures above, those samples, except Sample 7, all have a relatively small size (ranged from 5~12nm) and disperse uniformly in the liquid. However, in Sample 7, which is the ATO, most of the ATO particles aggregate and then the size is more than 2 µm. It seems like they all corresponded to the calculated value listed in Table. 2 besides Sample 7. The huge particle displayed in Fig. 2g is the aggregation of lots of separated ATO nano

particles. In HRTEM of Sample 7, the crystal particle size is about 12 nm. Thus, after associating with such $TiO_2$, ATO particles are dispersed much more uniformly and then they exist in the aqueous phase stably.

For the SAED pictures above, the diffraction rings in Sample 1 represent the crystalline interplanar spacing (namely, d) of 0.350, 0.242, 0.190, 0.170, 0.149, 0.136, 0.127 nm respectively. They exactly correspond to the anatase $TiO_2$ crystal face (101), (103), (200), (105), (213), (116) and (107). The (200) and (004) are also detected in HRTEM. However, in the following samples, with the decreasing of $TiO_2$, diffraction rings belonging to $SnO_2$ start to appear. In Sample 2, (110) of $SnO_2$ and (103), (105) of anatase $TiO_2$ are displayed and they are also shown in HGTEM. In the following samples, more and more $SnO_2$ diffraction rings appear while those of $TiO_2$ are fading until disappear. In Sample 3 and Sample 4, there are two obvious and close rings. The inner one represents the (101) of $TiO_2$ and the outer one represents the (110) of $SnO_2$. The HRTEM also shows the crystal faces belonging to those two compounds respectively. But starting from Sample 5, $TiO_2$ cannot be detected in SAED or HRTEM. Compared with XRD, TEM is more precise since in the XRD results, there are no characteristic peaks of $TiO_2$ from Sample 2 to Sample 6.

After the TEM tests, conclusions can be drawn that this method produces a fine dispersed and stable aqueous ATO sample whose particle size ranges from 5~12 nm. With the increasing of ATO concentration, the diffraction rings of $TiO_2$ and $SnO_2$ are

detected simultaneously. However, the crystallinity of $TiO_2$ is weaker than $SnO_2$ in this condition, thus the diffraction rings of $TiO_2$ are not detected since Sample 5.

## 4.3. The XPS characterizations

To confirm the chemical composition, the XPS characterizations are conducted. In this section, only sample 6 is detected. The full scanned spectrum is shown in Fig. 3a. In this figure, the characteristic peaks of C1s and Ti2p appears at 284.6 eV and 459.62 eV respectively. The characteristic peaks of Sn3d, Sn3d5 and Sn3p3 are shown at 486.8 eV, 494.49 eV and 716.72 eV respectively. The O1s peak overlap the Sb3d peak, therefore only a big strong peak appears at 530.88 eV. The high resolution XPS spectrum of Ti2p and Sn3d are shown in Fig. 3b and c respectively. The peak at 458.84 eV represents the $Ti2p_{3/2}$ and the other one located at 464.48 eV was assigned to $Ti2p_{1/2}$. The splitting between $Ti2p_{3/2}$ and $Ti2p_{1/2}$ is 5.64 eV, indicating a normal state of $Ti^{4+}$ in the $TiO_2$/ATO composite nano particles. In Fig. 3c, because of the spin-orbital splits, the Sn3d5/2 and Sn3d3/2 peaks also have characteristic double peaks at binding energies of 486.8 eV and 495.28 eV respectively. The splitting between them is 8.48 eV, representing a normal state of $Sn^{4+}$ in the composite nano particles. In another aspect, the main factor effecting the electrical conductivity of ATO is the molar ratio of $Sb^{5+}$ and $Sb^{3+}$. Hanse, the peak of $Sb3d_{3/2}$ is split to evaluate the molar ratio of $Sb^{5+}$ and $Sb^{3+}$. As shown in Fig. 3d, the peak at 540.59 eV is assigned to the $Sb3d_{3/2}$ orbital of supported $Sb^{5+}$ and the peak at 539.9 eV is assigned to the Sb3d3/2 orbital of supported Sb3+.

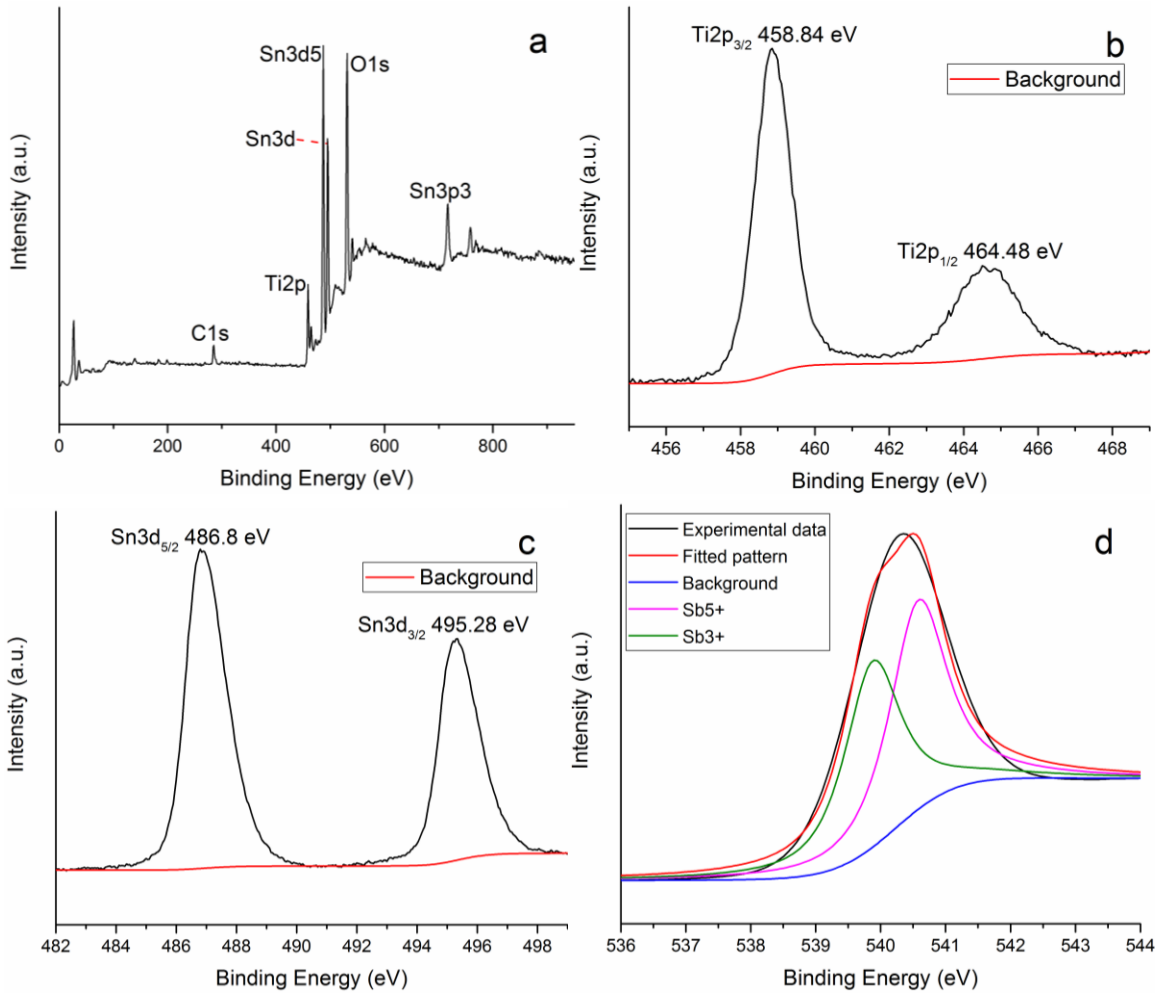


Fig. 3 (a) XPS full scanned spectrum of $TiO_2$/ATO composite nano particles. (b) The high resolution XPS spectrum of Ti2p. (c) The high resolution XPS spectrum of Sn3d. (d) The splitting peaks of $Sb3d_{3/2}$.

The relative area of peak represents the content of the valence state, the larger the area, the more content of the valence state. In Fig. 3d, the ratio of the peak areas of $Sb^{5+}$ and $Sb^{3+}$ is 1.13. Based on XPS characterizations, the $TiO_2$/ATO composite nano particles are successfully synthesized. The Ti and Sn exists as $Ti^{4+}$ and $Sn^{4+}$. However, the Sb consists of $Sb^{5+}$ and $Sb^{3+}$ and their molar ratio is 1.13.

## 4.4. The FT-IR and TGA characterizations

The FT-IR tests are then processed. The FT-IR patterns are shown in Fig. 4a below. As shown in this figure, all the curves are relatively smooth and have only a few peaks. It can be inferred that the compositions of those samples are relatively simple and there are only a few functional groups. In another word, the organic composition is relatively low.

As shown in the curve of Sample 1, which is the pure $TiO_2$, the peaks around 500 $cm^{-1}$ represent the characteristic IR absorption peak of Ti-O. The peaks at around 3348 $cm^{-1}$ and 1629 $cm^{-1}$ are the widest and strongest. Those two represent the antisymmetric stretching vibration peaks of H-O-H groups. This is related to the water adsorption and the surface hydroxyls. Since the crystal structure of mixed particles does not change based on the results from the XRD and TEM, $TiO_2$ and ATO are considered to bond together by the H-O-H bond, which is caused by the condensation of -OH on their surface. From Sample 1 to Sample 6, with the gradually decreasing of $TiO_2$, the FT-IR spectra change gradually. They all show the broad peaks at around 3348 $cm^{-1}$, and the peaks at 1629 $cm^{-1}$ and 1380 $cm^{-1}$. Besides the peaks at around 3348 $cm^{-1}$ and 1629 $cm^{-1}$ mentioned above, the peaks at around 1380 $cm^{-1}$ represent the $-CH_2-$ group. It is probably the organic residual in original ATO particles since it is not displayed in Sample 1 curve. Moreover, the peaks around 500~750 $cm^{-1}$ not only represent the vibration peaks of Ti-O bond but also the Sn-O bond. However, for Sample 7, which is the original ATO sample, there are no peaks in this curve. This is because ATO has an excellent property of

absorbing IR radiation. Thus, some characteristic peaks of its inherent groups cannot be detected.

It also caused that, the strength of the peaks at 1380 $cm^{-1}$ from Sample 2 to Sample 7 gradually fade and even disappeared in Sample 7. When ATO concentration reduces, the IR absorption is weakening too. Therefore, the signals of some groups can be detected. Besides, with the gradually decreasing strength of the peaks at around 3348 $cm^{-1}$ and 1629 $cm^{-1}$, the concentration of $TiO_2$ can be considered decreasing as well.

Therefore, it is inferred that there are limited organic compounds in those samples. This is confirmed by the following TG tests. Additionally, the pure ATO sample FT-IR curve shows an excellent IR absorption property. Besides the gaining of IR absorption property caused by gradually increasing ATO concentration, the reducing $TiO_2$ also gives rise to the gradually weaken hydroxy peaks at around 3348 $cm^{-1}$ and 1629 $cm^{-1}$.

Then the TGA (Thermogravimetric Analysis) is processed. Sample 4 is taken as an example since those samples are quite similar except the concentration difference. The result is shown in Fig. 4b below. It is apparent that the weight loss curve is quite flat and the total weight loss is less than 6% after heated to over 600 ℃. This means compounds in this sample are all quite thermal-stable. Therefore, associated with the FT-IR data above, conclusions can be draw that in the sample made in this way, barely no organic components are applied or remained.

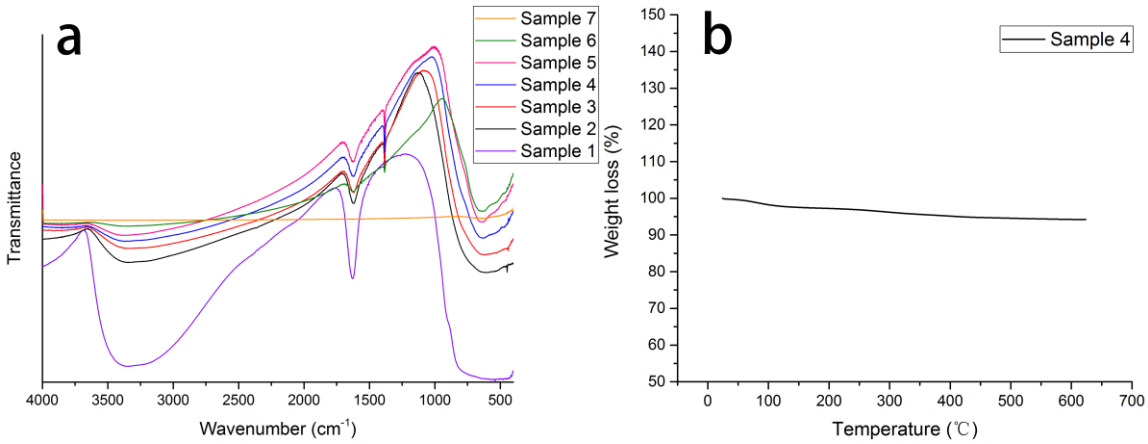


Fig. 4 The FT-IR results from Sample 1 to Sample 7 (a) and the TGA result of Sample 4 (b).

## 4.5. The particle distribution characterizations

After the FT-IR tests, the particle distribution tests are processed. The results are shown in Fig. 5. As shown in those curves, from Sample 1 to Sample 6, all of them have a similar particle distribution. Their size ranges from 10nm to 500nm and the D50 is about 50nm. For Sample 7, the size ranges from 1μm to 50 μm and the D50 is about 5 μm. All the values are larger than detected by TEM, it is because the results from TEM are the primary particle size but the particle distribution reviles the secondary particle size. In aqueous phase, the nano particles do not exist as a single separate particle. They must aggregate and absorb some particles with different electric charge and then form a slightly bigger colloid particle. In this case, those nano particles decrease enormous surface energy and then exist stably in aqueous phase. It is found out that, if ball-milled with high-dispersed $TiO_2$, the secondary particle size of ATO displays a huge decreasing

from around 5 μm to 50nm. It is a 100 times enhancement. Following that, to detect the stability of ATO/$TiO_2$ dispersing liquid, the Zeta potential tests are then processed.

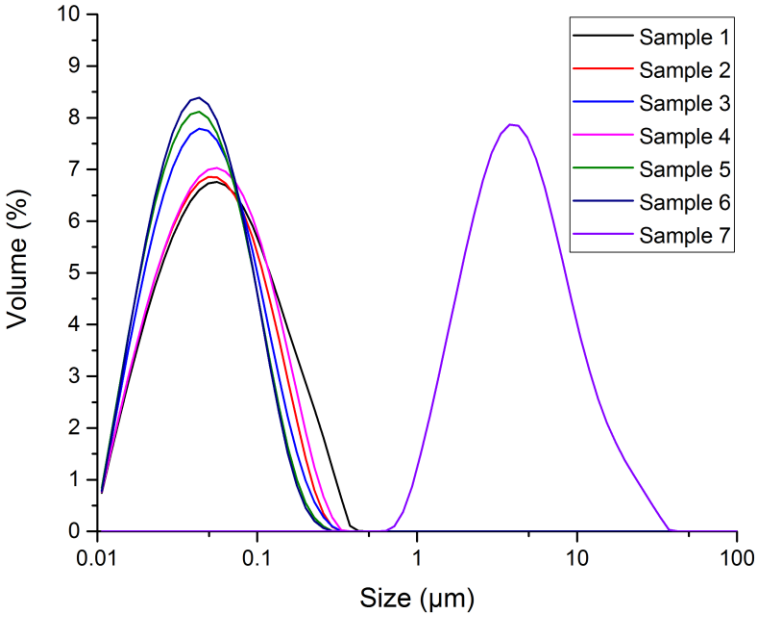


Fig. 5 The particle distribution results from Sample 1 to Sample 7.

## 4.6. The Zeta potential characterizations

The differences of those 7 samples are obvious. As shown in Fig. 6a, the macroscopic photo represents the dispersion effects. They are arranged in order from the left to right. With the increasing of ATO, the color turns more and more blue. For Sample 1 at the far left, it is milk white. This is the color of self-dispersed $TiO_2$. For the Sample 7 at the far right, the ATO particles aggregate and precipitate quickly.

Zeta potential is an important factor reflecting the stability of the colloid. In general, when it ranges from 0 to ±5, the colloid is so unstable that it precipitates rapidly; when it ranges from ±10 to ±30, the colloid is incipient instability; when it ranges from ±30 to

±40, the colloid is moderate stability; when it ranges from ±40 to ±60, the colloid is good stability and when it is more than ±60, the colloid is excellent stability. The Zeta potential is measured here. The result is shown in Fig. 6b. As shown in this figure, for the sample with 0% ATO, namely Sample 1, the Zeta potential is 41.76 mV. The stability is in the good level. With the increasing of ATO concentration, the Zeta potential is slightly decreasing from 41.76 mV in Sample 1 to 37.01 mV in Sample 6. They are all in a relatively good stability. However, when the ATO concentration is 100%, namely Sample 7, the Zeta potential decreases drastically to 6.7 mV. In this situation, the ATO particles are quite easy to aggregate and then precipitate. The results suggest that the $TiO_2$ contributes a lot to the dispersion of ATO particle in aqueous environment. A brief scheme is shown in Fig. 7.

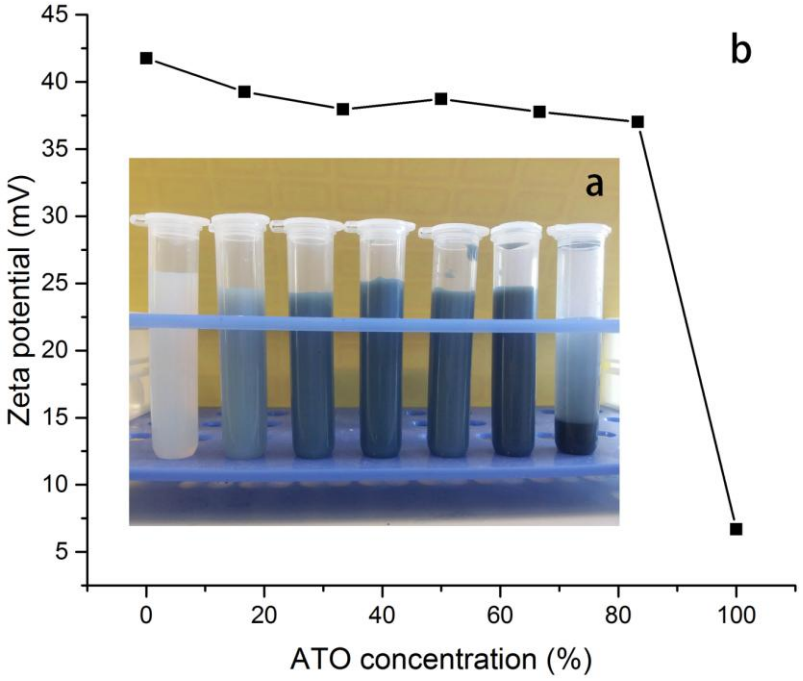


Fig. 6 The particle distribution results from Sample 1 to Sample 7

As shown in Fig. 7, the ATO/$TiO_2$ nano particles are bonded together via the -OH condensation on their surface. Then they form the core of the colloid particle and it is negatively charged. This is probably caused by the Cl- remaining on the $TiO_2$ surface since the titanium tetrachloride is the raw material. Then the positive ions are absorbed on the particle surface. This layer is called as Stern layer. Following that is the Slipping plane, which is the interface where the relative displacement between the colloid particle and the dispersion medium happen. Zeta potential is the potential difference between the Slipping plane and the dispersion medium. Therefore, the more the absolute Zeta potential value is, the more stable the colloidal solution is.

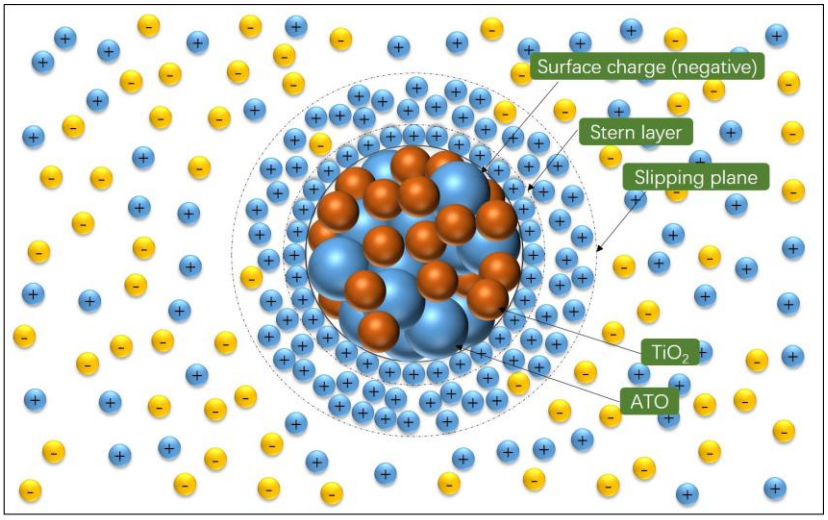


Fig. 7 The schematic sketch of the $TiO_2$/ATO colloids in aqueous dispersion.

## 4.7. The Vis-NIR characterizations

Then, the Vis-NIR transmittance characterizations are processed. As shown in Fig. 6b, because the ATO particles do not exist stably in Sample 7, it cannot form a uniform coating on a glass. Only first 6 samples and an original glass sheet are measured. Those samples are all firstly settled to the same solid content 5.0% wt. After the coating liquids are ready, the pulling method is applied to coat the film on the glass sheet. The speed is 0.5 cm/s and it lasted for 20 times. Then they are dried in room temperature. Since the coating thickness is an important parameter effecting the transmittance, the coating thickness is then measured which is shown in Fig. 8.

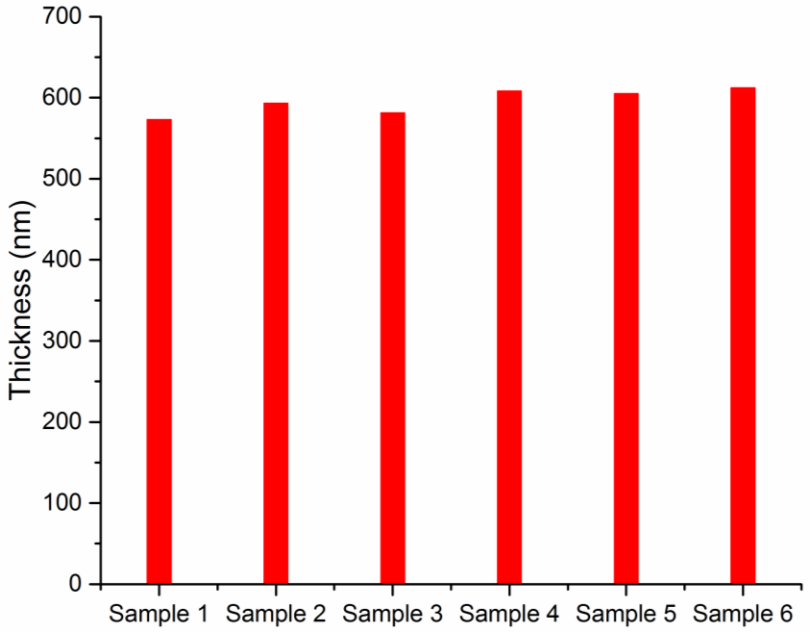


Fig. 8 The coating thickness of the first 6 coatings on the glass

In Fig. 8, it is found that the thickness values of those coating are quite similar. They all range from 573~612 nm. Then the Vis-NIR tests are processed. The results are shown in Fig. 9. As shown in those curves, for Sample 1, there is a slightly decrease than the

original glass, this is because firstly anatase $TiO_2$ can reflect part of the IR and secondly the coating film also influenced the transmittance of visible light. From Sample 2 to Sample 6, with the increasing of ATO concentration, the transmittance in NIR band (780~2500 nm) is decreasing gradually. For original glass, the transmittance is about 90% and for Sample 6 it decreases to about 1~2%. This means that the ATO does help to absorb the NIR, and the more the ATO concentration is, the better the IR insulation property is. Furthermore, it also can be revealed that the ATO shows a better IR insulation property than $TiO_2$. For Sample 1, there is barely no IR insulating, but all the other samples show better IR blocking property. $TiO_2$ does not obviously display this property.

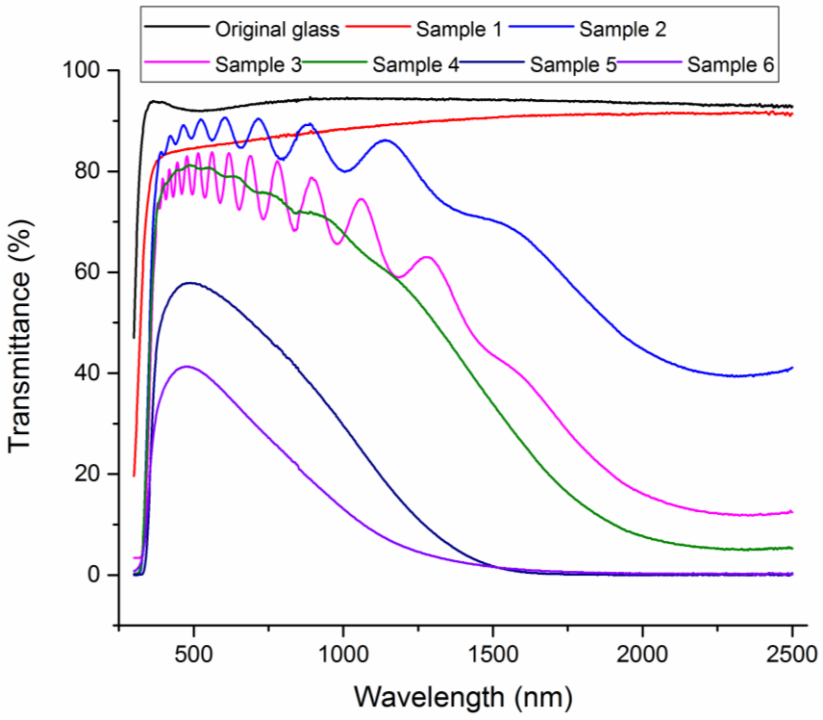


Fig. 9 The Vis-NIR transmittance results from Sample 1 to Sample 6. The incident light wave length ranges from 300~2500 nm. In all tests, air is the background.

## 4.8. The heat insulation simulation

To detect the heat insulation property quantificationally, the simulation is conducted. Energy Plus 8.3 is selected as the simulation software. A typical office room model has been created for simulation as shown in Fig. 10. The dimension is 4 m(H)*4 m(W)*3 m(L). The window is installed in the south wall and located 1 m above the ground. Its size is 3x1.5 m. This office room model has only one external wall while other surfaces are designed to separate thermal zones with the same conditions. After the model is built, the transmittance data of those samples are input to the software.

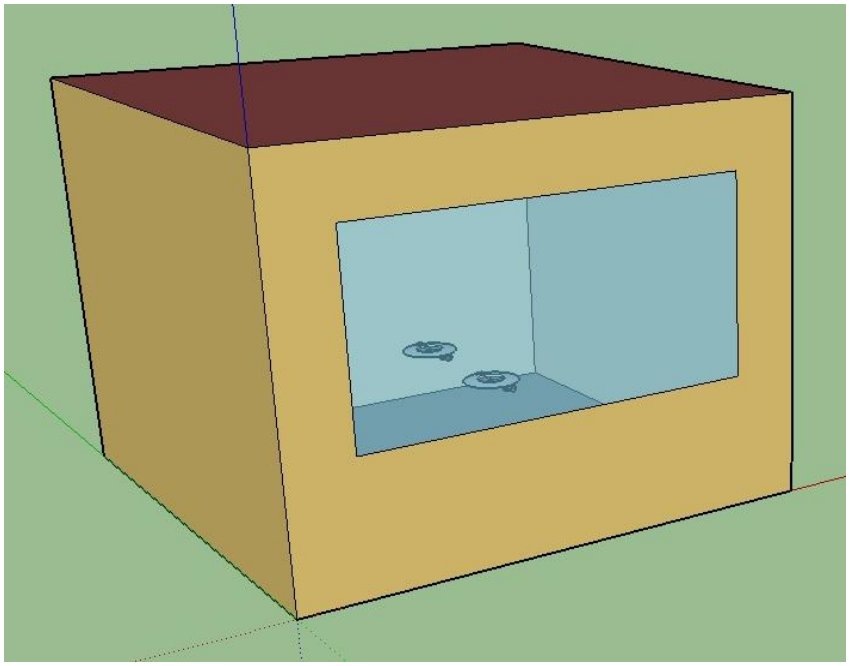

Fig. 10 An office room model for simulating the heat insulation property of the samples made above. The dimension of this room is 4 m(H)*4 m(W)*3 m(L). The window opening is located 1 m above the ground on the south facing wall and its area is 3x1.5 m.

Fig. 11 and Fig. 12 represent the window heat gain energy and the window transmitted solar radiation respectively. The former one means the energy obtained from the window and the latter one represents the solar energy transmitted this very window. Those two figures have a quite similar trend. Starting from January, the window heat gain energy and the window transmitted solar radiation decrease until reach the bottom in May or June. Then, they increase until December. Such trends are due to the Hong Kong climate situation. Window heat gain energy is closely related to the transmitted solar radiation. In general, most of the window heat gain comes from the transmitted solar radiation.

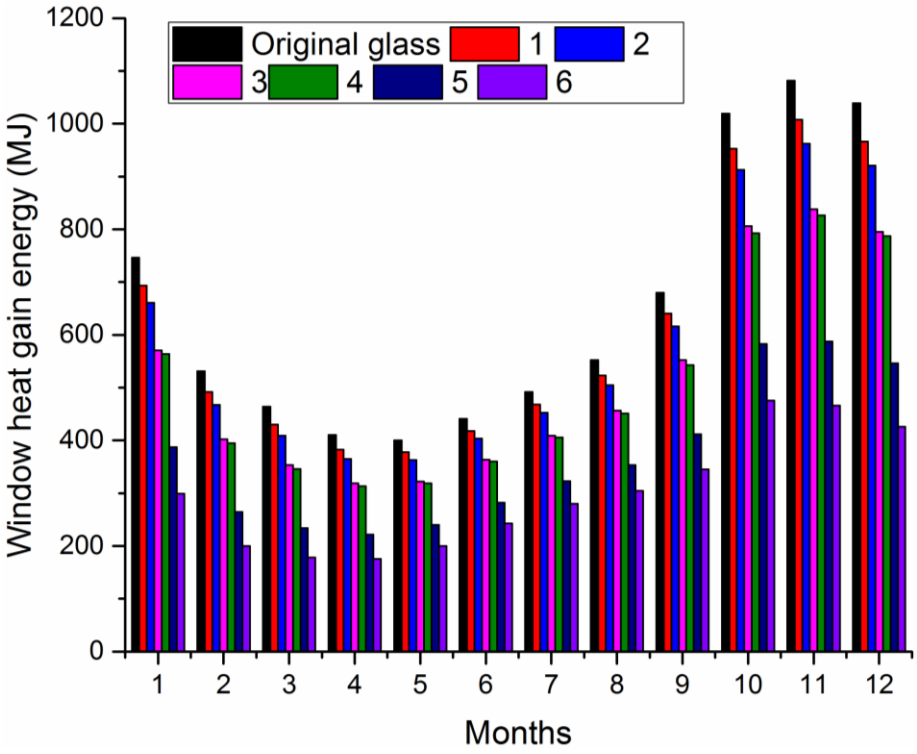


Fig. 11 The window heat gain energy of those samples. The results are from January to December.

If comparing those 7 samples, the original glass has the highest window heat gain energy and transmitted solar radiation in each month. With the increasing of ATO concentration, the window heat gain energy and transmitted solar radiation decrease. They both reach the lowest values in sample 6. It demonstrates that the ATO does block the solar radiation and decrease the heat obtained from the window.

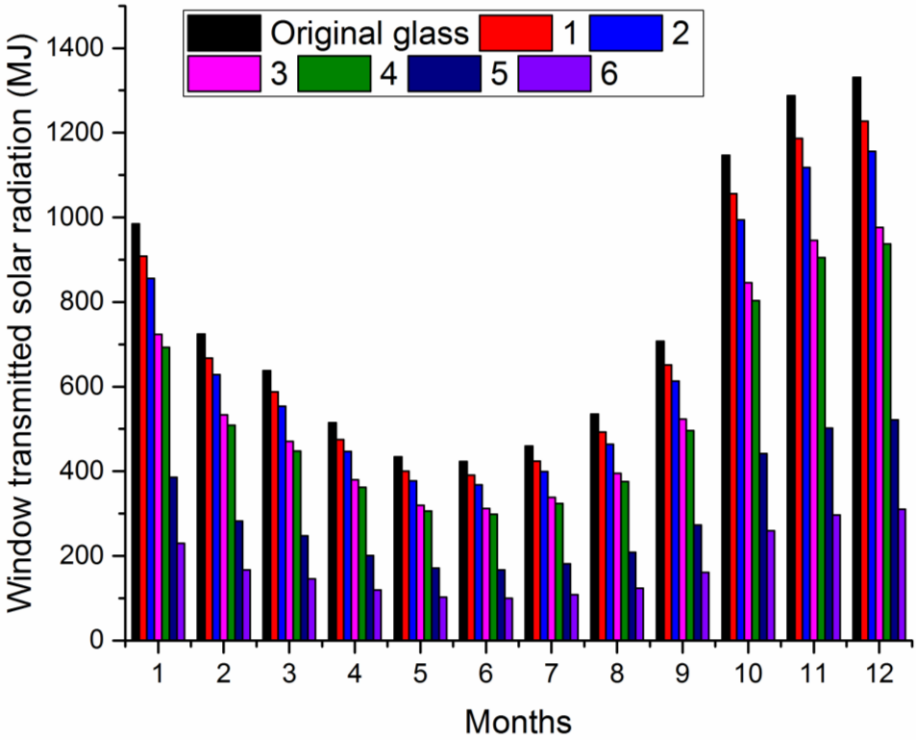


Fig. 12 The window transmitted solar radiation of those samples. The results are obtained from January to December.

As shown in Fig. 13, in the simulation results, the glass inside surface temperature and room temperature of those samples in 1$^{st}$ Jan are compared. In both figures, each sample reaches the highest value at 14 o'clock or 15 o'clock, which is the highest time in one day. In Fig. 13a, the original glass has the lowest glass inside surface temperature and the No.

6 sample shows the highest temperature from ca. 9 o'clock to 16 o'clock, which is the time with sufficient sunshine. Also, the trend is higher ATO concentration, higher inside surface temperature. This is because most of the IR in the sunlight is absorbed by this coating. With higher ATO concentration, more IR is absorbed. The absorbed IR transfers to heat. Therefore, the glass temperature increases with the increasing of ATO concentration. On the other hand, when there is no sufficient sunlight, the thermal conduction and thermal convection are the main factors effecting the glass inside surface temperature. As shown in Fig. 13b, the room temperature with coated glass shows big decrease when compared with original glass. With higher ATO concentration, the more the room temperature decreases. Therefore, when the sunlight is not sufficient, the glass inside surface temperature is inverse proportion to the ATO concentration. In Fig. 13b, for sample 6, the highest temperature is 6 ℃ lower than original glass. The difference is obvious. Based on this simulation, it is demonstrated that such coating does help to decrease the room temperature.

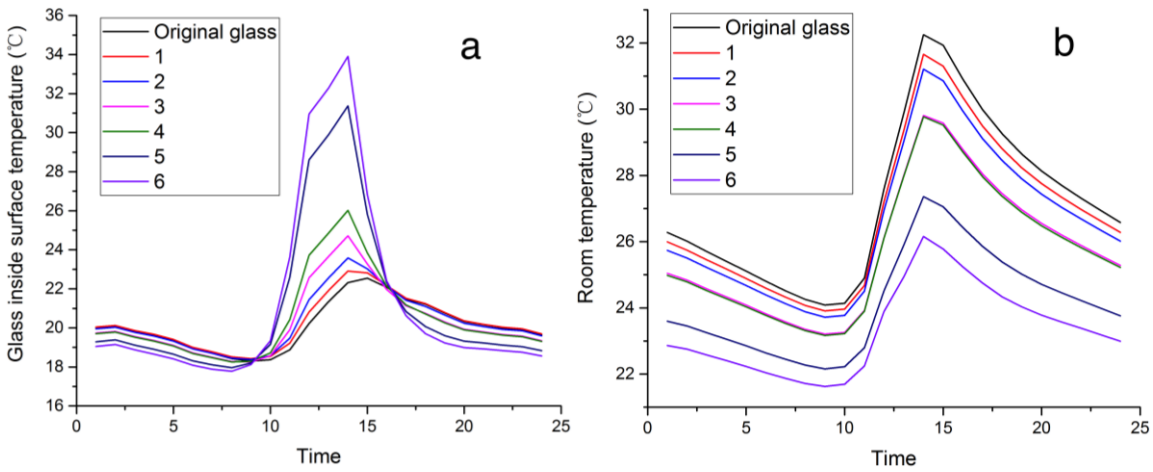


Fig. 13 The glass inside surface temperature (a) and room temperature (b) of those samples in 1st Jan.

The annual energy use of air-conditioning (AC) and lighting are demonstrated in Fig. 14. As displayed in Fig. 9, even though the increasing of ATO concentration influence the transmittance of visible light, the electricity use of lighting is not largely gained. The AC electricity consumption decreases with the gaining of ATO concentration. Compared with original glass (1289 kWh), the total electricity use of sample 6 (933 kWh) is 27% lower.

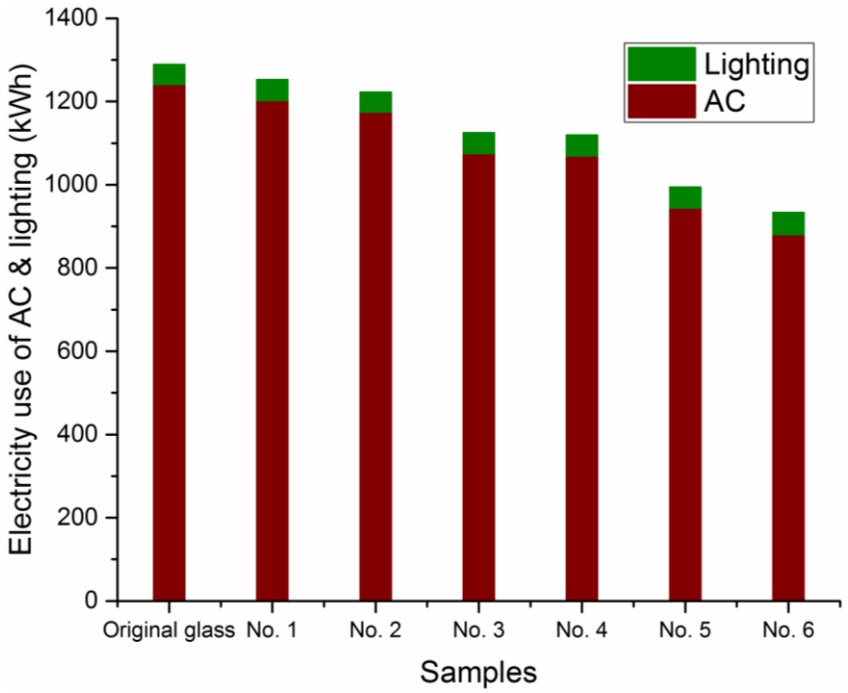


Fig. 14 The electricity use of AC and lighting of those samples. The green columns represent the electricity use of lighting and the wine ones represent the AC.

## 4.9. The contact angle characterizations

Those samples are coated on a glass sheet firstly, then the contact angle (CA) characterizations of those samples are then processed. The results are shown in Fig. 15. As shown in those figures, the CA of original glass is 59°. But from Sample 1 to Sample 6, the CA value ranges from 3.0~6.0° which represents that the super-hydrophilic surface is formed. This is boiled down to the anatase $TiO_2$ in those particles since the super-hydrophilic property derives from $TiO_2$. For the sample without $TiO_2$, namely Sample 7, the CA is 41° which is slightly smaller than the original glass sheet. It is because in Sample 7, most of the ATO particles aggregate and form some micro-pores on the glass. Because of the capillary effect, some water is absorbed and then the CA

decreases slightly. Therefore, in this chapter, conclusions can be drawn that the ATO/$TiO_2$ composed particles show the super-hydrophilicity and then the self-cleaning property is obtained. In this way, the lifetime of this coating is prolonged due to the anti-fouling surface.

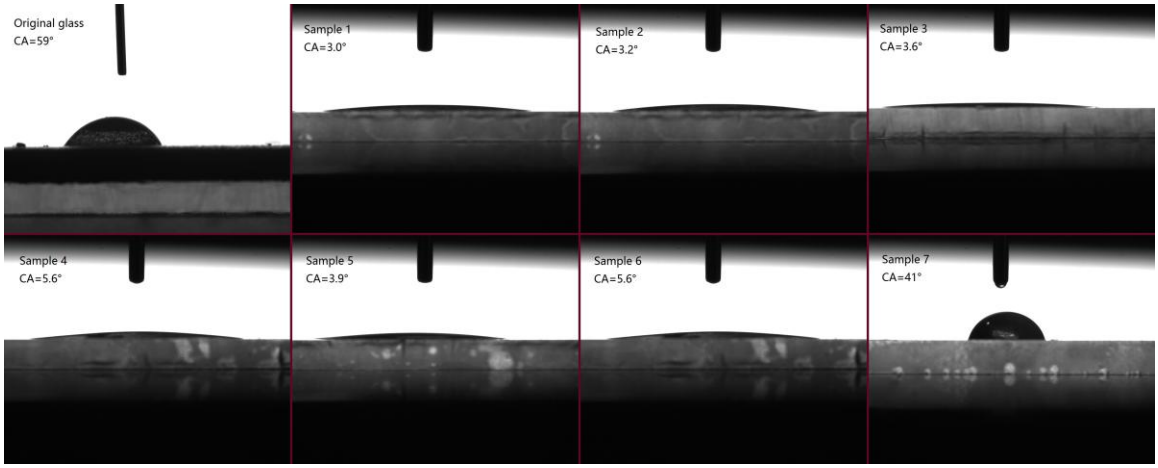


Fig. 15 The contact angle images of the glass with those samples

# 5. Conclusions

In this work, a highly dispersed aqueous $TiO_2$/ATO composites nano particles are synthesized. An inorganic self-dispersed $TiO_2$ is firstly produced by solvent-thermal method and then is used as the dispersion agent. $TiO_2$ and ATO are bonded together by the condensation of -OH groups on their surface. This method is quite environment-friendly since there are no organic compounds or organic solvent media applied. In this way, the Zeta potential of $TiO_2$/ATO dispersion samples ranges from ca. 37~40 mV. For comparison, that of the pure ATO is 6.7 mV. The addition of $TiO_2$ enhances the stability of the composite nano particles in aqueous phase drastically. In addition, the TEM images display the primary particle size of the $TiO_2$/ATO particles

range from 5~12nm, while for the pure ATO particles, the size is more than 2 μm. Similar results are obtained from the particle distribution characterizations. Besides the pure ATO sample (D50: 5 μm), all samples have a uniform size (D50: 50 nm). They are all slightly bigger than the primary particle size detected by TEM. This is because the particles must aggregate and then form a bigger colloid particle. In addition, through the XPS characterization, the ratio of $Sb^{5+}$ and $Sb^{3+}$ is calculated and the value is 1.13. Moreover, such coating displays a good property of IR insulation. In NIR band, the transmittance decreases from ca. 90% (original glass) to ca. 1~2% (Sample 6). Based on such optical properties, the thermal performances of the glass with those coatings are simulated. From the results, those coating indeed decrease the room temperature. With higher ATO concentration, the better thermal insulation performance it is. For the sample with highest one (83.3% wt.), the room temperature is 6 ℃ lower than original glass when it is the hottest time in a day. The electricity used in AC and lighting is also decreased. Compared with original glass, the sample with highest ATO concentration saves 27% electricity. Other than that, since $TiO_2$ is applied, the coating also shows the super-hydrophilicity. Therefore, self-cleaning property is endowed to such coating. Then, the life time is pro-longed since most of the dust must be washed away by the self-cleaning coating.

# Acknowledgements

The work described in this paper was supported by a grant from the CII-HK / PolyU Innovation Fund. The great help from Department of Applied Biology & Chemical Technology of The Hong Kong Polytechnic University and The Hong Kong Polytechnic University Research Institute for Sustainable Urban Development (RISUD) is appreciated. This work is also supported by Shenzhen Peacock Plan (KQTD2015071616442225). Finally, we would like to acknowledge the partially financial supports from Hong Kong Innovation Technology Commission through ITF project UIM/265.

[1] Pérez-Lombard L, Ortiz J, Pout C. A review on buildings energy consumption information[J]. Energy and buildings, 2008, 40(3): 394-398.

[2] Emery K, Myers D. Reference solar spectral irradiance: air mass 1.5[J]. Center, RERD, Ed, 2009.

[3] Arfsten N J. Sol-gel derived transparent IR-reflecting ITO semiconductor coatings and future applications[J]. Journal of Non-Crystalline Solids, 1984, 63(1): 243-249.

[4] Ravichandran K, Muruganantham G, Sakthivel B. Highly conducting and crystalline doubly doped tin oxide films fabricated using a low-cost and simplified spray technique[J]. Physica B: Condensed Matter, 2009, 404(21): 4299-4302.

[5] Mulla I S, Soni H S, Rao V J, Sinha A P B. Deposition of improved optically selective conductive tin oxide films by spray pyrolysis[J]. Journal of materials science, 1986, 21(4): 1280-1288.

[6] Guo J, She C, Lian T. Ultrafast electron transfer between molecule adsorbate and antimony doped tin oxide (ATO) nanoparticles[J]. The Journal of Physical Chemistry B, 2005, 109(15): 7095-7102.

[7] Peaker A R, Horsley B. Transparent conducting films of Antimony doped tin oxide on glass[J]. Review of Scientific Instruments, 1971, 42(12): 1825-1827.

[8] Dai Z, Li Z, Li L, Xu G. Synthesis and thermal properties of antimony doped tin oxide/waterborne polyurethane nanocomposite films as heat insulating materials[J]. Polymers for Advanced Technologies, 2011, 22(12): 1905-1911.

[9] Castro M R S, Schmidt H K. Transparent conducting antimony‐doped tin oxide films containing functionalized multi‐walled carbon nanotubes[J]. Physica status solidi (a), 2007, 204(10): 3380-3386.

[10] Zhang J, Gao L. Synthesis and characterization of antimony-doped tin oxide (ATO) nanoparticles[J]. Inorganic Chemistry Communications, 2004, 7(1): 91-93.

[11] Jeon H J, Jeon M K, Kang M, Lee S G, Lee Y L, Hong Y K, Choi B H. Synthesis and characterization of antimony-doped tin oxide (ATO) with nanometer-sized particles and their conductivities[J]. Materials Letters, 2005, 59(14): 1801-1810.

[12] Tatyana D, Victor I, Valentina V, Roman A. Method for Determining the Doping Efficiency of Dispersed Semiconductor Metal Oxide Materials[J]. Key Engineering Materials, 2016, 683.

[13] Kim D W, Kim D S, Kim Y G, Kim Y C, Oh S G. Preparation of hard agglomerates free and weakly agglomerated antimony doped tin oxide (ATO) nanoparticles by coprecipitation reaction in methanol reaction medium[J]. Materials chemistry and physics, 2006, 97(2): 452-457.

[14] Liu T J, Jin Z G, Feng L R, Wang T. Conducting antimony-doped tin oxide films derived from stannous oxalate by aqueous sol–gel method[J]. Applied Surface Science, 2008, 254(20): 6547-6553.

[15] Zhang J, Gao L. Synthesis and characterization of antimony-doped tin oxide (ATO) nanoparticles by a new hydrothermal method[J]. Materials chemistry and physics, 2004, 87(1): 10-13.

[16] Bai F, He Y, He P, Tang Y, Jia Z. One-step synthesis of monodispersed antimony-doped tin oxide suspension[J]. Materials Letters, 2006, 60(25): 3126-3129.

[17] Coleman J P, Lynch A T, Madhukar P, Wagenknecht J H. Antimony-doped tin oxide powders: Electrochromic materials for printed displays[J]. Solar energy materials and solar cells, 1999, 56(3): 375-394.

[18] Posthumus W, Laven J, de With G, van der Linde R. Control of the electrical conductivity of composites of antimony doped tin oxide (ATO) nanoparticles and acrylate by grafting of 3-methacryloxypropyltrimethoxysilane (MPS)[J]. Journal of colloid and interface science, 2006, 304(2): 394-401.

[19] Posthumus W, Magusin P, Brokken-Zijp J C M, Tinnemans A H A, van der Linde R. Surface modification of oxidic nanoparticles using 3-methacryloxypropyltrimethoxysilane[J]. Journal of colloid and interface science, 2004, 269(1): 109-116.

[20] Chen X, Li C, Shao W, Liu T, Wang L. Nonisothermal crystallization kinetics of poly (ethylene terephthalate)/antimony‐doped tin oxide nanocomposites[J]. Journal of applied polymer science, 2008, 109(6): 3753-3762.

[21] Cho Y S, Kim H M, Hong J J, Yi G R, Jang S H, Yang S M. Dispersion stabilization of conductive transparent oxide nanoparticles[J]. Colloids and Surfaces A: Physicochemical and Engineering Aspects, 2009, 336(1): 88-98.

[22] Carp O, Huisman C L, Reller A. Photoinduced reactivity of titanium dioxide[J]. Progress in solid state chemistry, 2004, 32(1): 33-177.

[23] Fujishima A, Rao T N, Tryk D A. Titanium dioxide photocatalysis[J]. Journal of Photochemistry and Photobiology C: Photochemistry Reviews, 2000, 1(1): 1-21.

[24] Ohko Y, Saitoh S, Tatsuma T, Fujishima A. Photoelectrochemical anticorrosion and self-cleaning effects of a TiO2 coating for type 304 stainless steel[J]. Journal of the Electrochemical Society, 2001, 148(1): B24-B28.

[25] Yan H, Yuanhao W, Hongxing Y. TEOS/silane coupling agent composed double layers structure: A novel super-hydrophilic coating with controllable water contact angle value[J]. Applied Energy, 2015.

[26] Fujishima A. Electrochemical photolysis of water at a semiconductor electrode[J]. nature, 1972, 238: 37-38.

[27] Hoffmann M R, Martin S T, Choi W, Bahnemann D W. Environmental applications of semiconductor photocatalysis[J]. Chemical reviews, 1995, 95(1): 69-96.

[28] Chen X, Mao S S. Titanium dioxide nanomaterials: synthesis, properties, modifications, and applications[J]. Chemical reviews, 2007, 107(7): 2891-2959.

[29] Scherrer P. Bestimmung der Grösse und der inneren Struktur von Kolloidteilchen mittels Röntgenstrahlen[J]. Nachrichten von der Gesellschaft der Wissenschaften zu Göttingen, mathematisch-physikalische Klasse, 1918, 1918: 98-100.